Toric AdS$_4$/CFT$_3$ duals and M-theory crystals

Sangmin Lee and Sungjay Lee

School of Physics and Astronomy, Seoul National University,
Seoul 151-747, Korea
E-mail: `sangmin@snu.ac.kr`, `saintlee@phya.snu.ac.kr`

Jaemo Park

Department of Physics, Postech,
Pohang 790-784, Korea
E-mail: `jaemo@physics.postech.ac.kr`

ABSTRACT: We study the recently proposed crystal model for three dimensional supercon-formal field theories arising from M2-branes probing toric Calabi-Yau four-fold singularities. We explain the algorithms mapping a toric Calabi-Yau to a crystal and vice versa, and show how the spectrum of BPS meson states fits into the crystal model.

Contents

1. Introduction

The brane tiling model $[1-6]$, a.k.a. dimer model, has proved to be a powerful tool to analyze the class of four dimensional, superconformal quiver gauge theories arising from D3-branes probing toric Calabi-Yau three-fold (CY_3) cones. Over the past few years, systematic methods that map a brane tiling to the associated toric CY_3 cone (forward algorithm [1]) and vice versa (inverse algorithm [4, 5]) have been firmly established. The brane tiling model has been used to study aspects of the quiver gauge theories such as marginal deformations $[7-9]$, counting BPS states $[10-18]$, and partial Higgsing $[2, 19-21]$. It has also found interesting applications to the recent study of supersymmetry breaking of metastable vacua and their embedding into string theory $[22-24]$.

Recently, the idea of the brane tiling model was applied to three dimensional superconformal theories arising from M2-banes probing toric CY_4 cones [25]. A three dimensional counterpart of the tiling model emerged and was named a crystal model. Throughout this
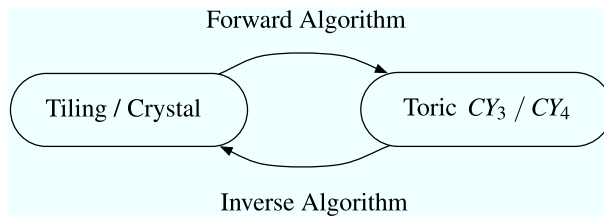
Figure 1: The forward/inverse algorithms.

paper, we will distinguish the D3/CY$_3$ model from the M2/CY$_4$ model by referring to the former as the tiling model and the latter as the crystal model. The notion of a dimer is equally relevant to both models.

The goal of this paper is to elaborate on the properties of the crystal model. We begin with a brief review of the construction of the crystal model [25] in section 2. In sections 3 and 4, we generalize the inverse/forward algorithms of the tiling model to the crystal model. We find that the forward algorithm can be carried over to the crystal model with little modification. The inverse algorithm also shares many essential features with that of the tiling model, but there are some crucial differences that require additional work. In section 5, we show in detail how the crystal model correctly reproduces the spectrum of the BPS meson states. We conclude with some discussions in section 6.

2. Review of the crystal model

We begin with a stack of N M2-branes near the tip of a CY$_4$ cone X. In the near horizon limit, the $\mathbb{R}^{1,2}$ world-volume directions of the M2-branes and the radial direction of X merge to form an AdS$_4$ and the base (unit radius section) of X becomes the internal 7-manifold Y. We say X is the cone over Y, or $X = C(Y)$. The crystal model assumes that X is toric, so we first recall some relevant aspects of toric geometry. See, for example, [26, 27, 14] for more information on toric geometry in this context.

2.1 Toric CY$_4$

We follow the notation of [25, 28] for toric geometry. The CY$_4$ cone X is a quotient of $\mathbb{C}^d$ for some $d \geq 4$. Given some integer-valued charge matrix Q_a^I ($I = 1, \cdots, d; a = 1, \cdots, d-4$), the quotient is taken by

$$X = \left\{ \sum_I Q_a^I |Z_I|^2 = 0 \right\} / (Z_I \sim e^{Q_a^I \theta^a} Z_I). \tag{2.1}$$

The toric diagram is a convex polyhedron composed of a set of lattice points $\{v_I^i\} \in \mathbb{Z}^4$ ($i = 1, \cdots, 4$) satisfying

$$\sum_I Q_a^I v_I^i = 0. \tag{2.2}$$
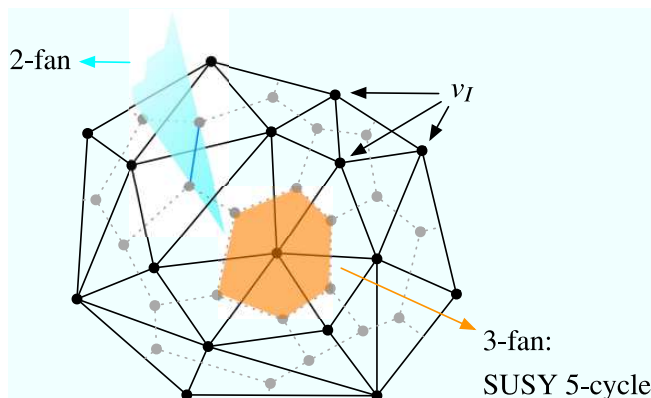
Figure 2: A toric diagram (solid line) is a convex polyhedron with integer-valued vertices in $\mathbb{R}^3$. Its graph dual (dotted line) gives the fan diagram.

The CY condition is $\sum_I Q_a^I = 0$, which leads the v_I to be on the same $\mathbb{Z}^3$ subspace. It is customary to choose a basis to set $v_I^4 = 1$ for all I.

The toric diagram defines a solid cone $\Delta \equiv \{y_i \in \mathbb{R}^4; (v_I \cdot y) \geq 0 \text{ for all } I\}$. We call the boundary components $S^I \equiv \Delta \cap \{v_I \cdot y = 0\}$ the 3-fans. Two 3-fans meet at a 2-fan and several 2-fans join at a 1-fan. These fans are graph dual to the original toric diagram in the sense that each vertex v_I is associated to a 3-fan, each edge connecting two neighboring vertices, $w_{IJ} = v_I - v_J$, corresponds to a 2-fan, etc. The cone X is a T^4 fibration over Δ. The fiber is aligned with the base in such a way that it shrinks to T^n on the n-fans.

The moduli space of Kähler metrics on X is parameterized by the Reeb vector $b^i \in \mathbb{R}^4$, which defines the base of the cone by $Y = X \cap \{b \cdot y = 1/2\}$. In the basis mentioned above, the CY condition fixes $b^4 = 4$. The volume of Y as an explicit function of v_I and b is known [27, 10]. The Ricci-flat metric is obtained by minimizing the volume with respect to b^i with the range of $b^i/4$ being precisely the toric diagram.

For later purposes, we recall that a baryon in the CFT$_3$ is mapped via AdS/CFT to an M5-brane wrapping a supersymmetric 5-cycle of Y [29]. Each 3-fan S^I dual to a vertex v_I defines a 5-cycle which is the T^3 fibration over $S^I \cap \{b \cdot y = 1/2\}$. We abuse the notation a bit and use S^I to denote either the 3-fan or the 5-cycle depending on the context. It was shown in [3] that $H_5(Y, \mathbb{Z}) = \mathbb{Z}^{d-4}$ with d being the number of internal vertices in the toric diagram, and that a set of basis $\{\mathcal{C}^a\} \subset H_5(Y, \mathbb{Z})$ can be chosen such that that $S^I = Q_a^I \mathcal{C}^a$, where Q_a^I is precisely the charge matrix defining the CY$_4$. The baryons S^I are said to be charged under the baryonic symmetries Q_a. The baryons are also charged under the four U(1) isometries F_i of X, called the flavor symmetries. There are also $d - 4$ baryonic symmetries Q_a. We normalize the charges of the the baryons to be $F_i[S^I] \equiv N F_i^I$, $Q_a[S^I] \equiv N Q_a^I$ with N being the number of M2-branes. They satisfy the toric relations $v_I^i F_j^I = \delta_j^i$ and $v_I^i Q_a^I = 0$ [28]. The U(1)$_R$ charge is the linear combination of the flavor charges $R = \frac{1}{2} b^i F_i$, where b^i is the Reeb vector. The toric relations and the CY condition ($b^4 = 4$) implies that $\sum_I R^I = 2$ and $\sum_I F_i^I = 0$ for $i = 1, 2, 3$. The value of each R^I is proportional to the volume of S^I [29] and can be computed following [27, 14].
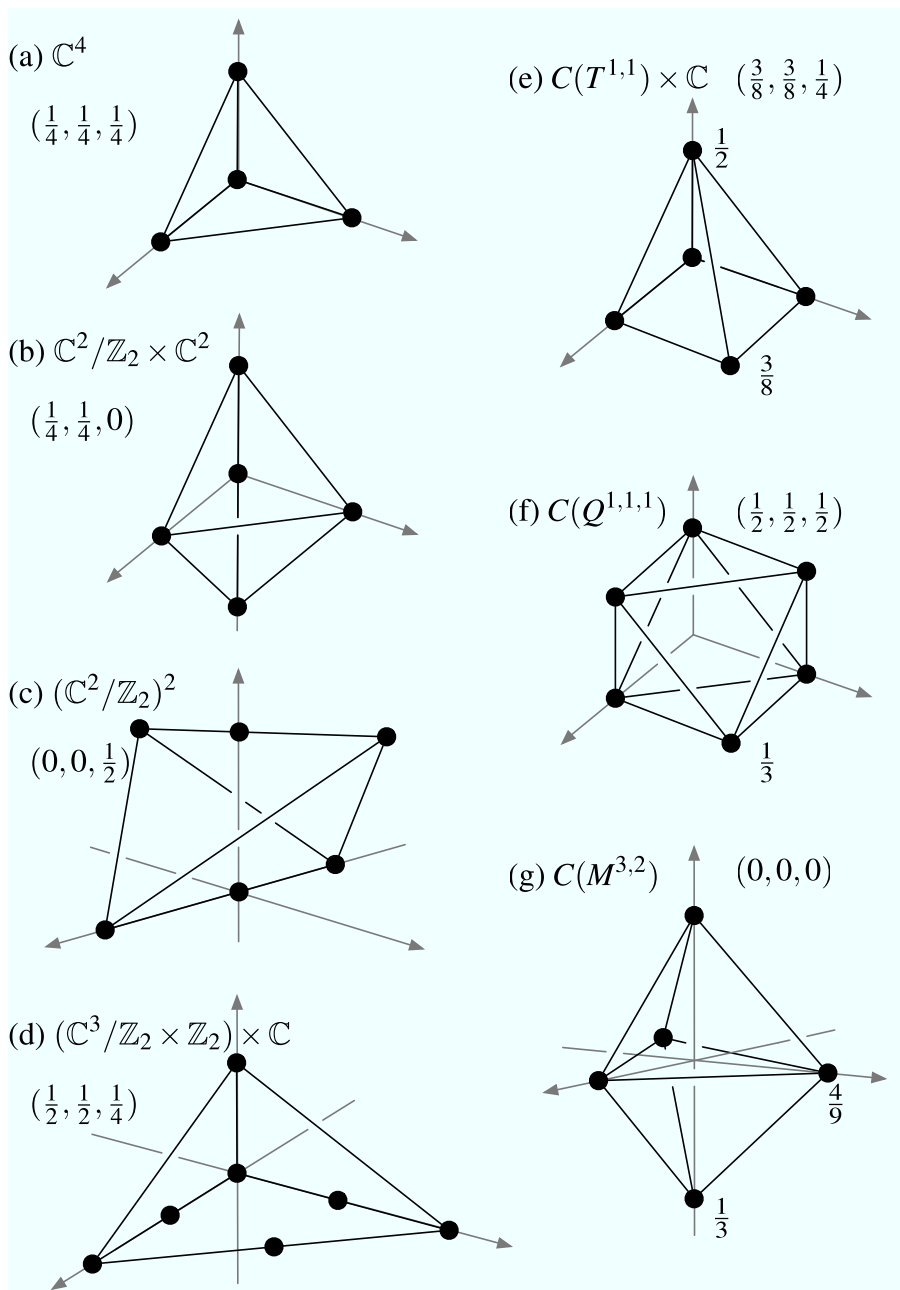
Figure 3: Toric diagrams, Reeb vectors and R-charges of some simple examples of CY_4.

Figure 3 lists the toric diagrams for the examples of CY_4 we will consider in this paper. The orbifolds in examples (b,c,d) are defined as follows. For $\mathbb{C}^2/\mathbb{Z}_2$, the $\mathbb{Z}_2$ group acts as $(z_1, z_2) \to (-z_1, -z_2)$. For $(\mathbb{C}^3/\mathbb{Z}_2 \times \mathbb{Z}_2) \times \mathbb{C}$, the two $\mathbb{Z}_2$ groups act on $\mathbb{C}^3$ as $(z_1, z_2, z_3) \to (-z_1, -z_2, z_3)$ and $(z_1, z_2, z_3) \to (z_1, -z_2, -z_3)$. In example (d), $C(T^{1,1})$ is the famous conifold whose base $T^{1,1}$ is the coset space $SU(2) \times SU(2)/U(1)$. Examples (e) and (f) are CY_4 counterparts of the conifold, in the sense that the base $Q^{1,1,1}$ and $M^{3,2}$ are

	0 1 2	3 4 5 6 7 8	9 11
M5	○ ○ ○	○ ○ ○	
M5	○ ○ ○	Σ	

Table 1: The brane configuration for the CFT$_3$. Away from the origin of $\mathbb{R}^3(345)$, the special Lagrangian manifold Σ is locally a product of a 2-plane in $\mathbb{R}^3(345)$ and a 1-cycle in $T^3(678)$.

coset spaces $\mathrm{SU}(2)^3/\mathrm{U}(1)^2$ and $\mathrm{SU}(3) \times \mathrm{SU}(2)/\mathrm{SU}(2) \times \mathrm{U}(1)$ [30]. They have been studied in the context of AdS/CFT correspondence in [31–38].

In figure 3, we included the Reeb vector components $b^i/4$ ($i = 1, 2, 3$) and the R-charges R^I of the baryons S^I. For $\mathbb{C}^4$ and its orbifolds, $R^I = 1/2$ for the four corners the toric diagrams and zero for other vertices. The R^I for the other three examples are written in the diagrams. Note that the vertices related by discrete symmetries have the same R^I.
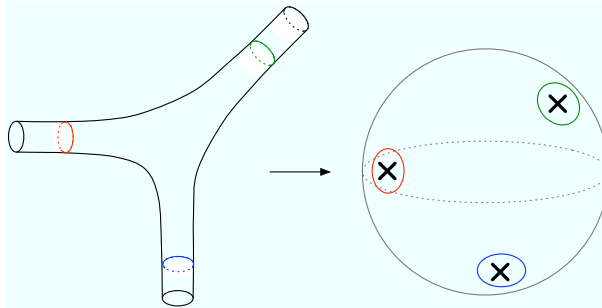
2.2 The crystal model

The crystal model follows from a T-duality of M-theory. It parallels the derivation of the tiling model using T-duality of IIB string theory [2, 39]. We take the T-duality transformation along $T^3 \subset T^4$ aligned with the $y_{1,2,3}$ coordinates. This corresponds to $x^{6,7,8}$ directions in table 1 below. By T-duality, we mean the element t in the $\mathrm{SL}(2, \mathbb{Z}) \times \mathrm{SL}(3, \mathbb{Z})$ duality group which acts as $t : \tau \equiv C_{(3)} + i\sqrt{g_{T^3}} \to -1/\tau$. The stack of N M2-branes turns into a stack of N M5-branes wrapping the dual T^3. We call them the T-branes. The degenerating circle fibers turn into another M5-brane extended along the (2+1)d world-volume and a non-trivial 3-manifold Σ in $\mathbb{R}^3 \times T^3$. We call it the Σ-brane. The result is summarized in table 1.

The brane configuration preserves supersymmetry if and only if the M5-branes wrap special Lagrangian submanifolds of $\mathbb{R}^3 \times T^3 = (\mathbb{C}^*)^3$. Clearly, the T-branes are special Lagrangian as it is calibrated by ImΩ, where Ω is the holomorphic three-form $\Omega = (dx^3 + idx^6) \wedge (dx^4 + idx^7) \wedge (dx^5 + idx^8)$. Demanding that the Σ-brane be calibrated by the same ImΩ, we learn that Σ is locally a plane in $\mathbb{R}^3$ and a 1-cycle in T^3. We will say more about the geometry of Σ in section 3.

In analogy with the tiling model, the content of the CFT$_3$ is expected to be encoded in the intersection locus between the T-branes and the Σ-brane projected onto the T^3. The result is a graph in the T^3 which we call the crystal lattice. As in the tiling model, the graph consists of edges and vertices which we call *bonds* and *atoms* to distinguish them from similar objects in the toric diagram. In [25], the simplest examples of the crystal were presented, and a few general properties of the inverse algorithm were stated without detailed explanation. We will study both the inverse and forward algorithms in sections 3 and 4, respectively, illustrating the ideas with the examples listed in figure 3.

One of the central result of [25] is that the fundamental excitations of the CFT$_3$ are the M2-discs whose boundary encircles the bonds of the crystal lattice. The derivation of the M2-disc picture made use of the smooth transition from a baryon to N fundamentals, inspired by a related work in the tiling model [39]. Using this picture, the super-potential terms and the F-term conditions of the crystal model were identified.

Figure 4: Amoeba for $\mathbb{C}^3$.

As an application of the crystal model, it was shown in [25] how to account for the spectrum of BPS meson operators using the M2-disc picture. In the original CY_4, the mesons are KK momentum modes. The T-duality transforms them into closed membranes. The R-charge and the flavor charges of a meson can be determined by decomposing it into elementary M2-discs. It is consistent with the known results on the BPS spectrum of chiral mesons from the geometry side [10 – 12]. In section 5, we will explain the details of this matching with explicit computations for a few examples.

3. Inverse algorithm

In this section, we generalize the inverse algorithm of the tiling model [4, 5] to the crystal model. The notion of amoeba and alga projections again plays an important role.

3.1 Review of the tiling model

In the tiling model, the T-duality maps the degenerating circle fibers into an NS5-brane wrapping a holomorphic surface Σ in $(\mathbb{C}^*)^2$. The surface is given by the Newton polynomial,

$$\sum_{(a,b)} c_{(a,b)} u^a v^b = 0, \qquad (u,v) \in (\mathbb{C}^*)^2. \tag{3.1}$$

where the sum runs over the vertices of the toric diagram. The projection of Σ onto $\mathbb{R}^2$ is called the amoeba and the projection onto T^2 is called the alga [5]. The amoeba is a thickened (p,q)-web. Each leg of the (p,q)-web asymptotes to a cylinder. If the legs get pulled in toward the center, the amoeba can be regarded as a punctured Riemann surface. The genus of the Riemann surface is equal to the number of internal points of the toric diagram [5].

The alga provides the key to the inverse algorithm. The boundaries of the alga are the 1-cycles associated to the legs of (p,q)-web. The tiling is obtained as the 1-cycles shrink into the interior of the alga and merge with one another. In practice, the inverse algorithm often works without actually taking the alga projection. One begins with drawing all 1-cycles and tries to shrink merge them to obtain a consistent tiling.

Since the alga and the amoeba are just two different projections of the same holomorphic surface, a simple map relating the two should exist. The map was found in [5]
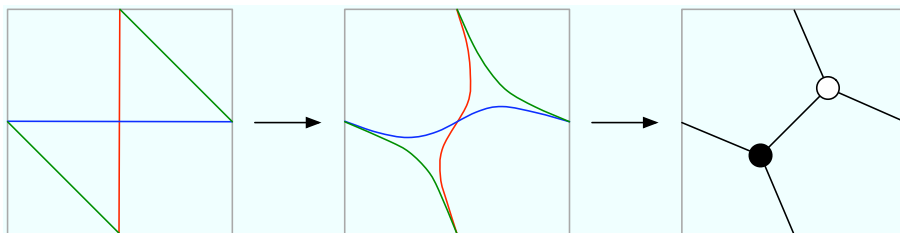
**Figure 5:** Alga and the inverse algorithm for $\mathbb{C}^3$.
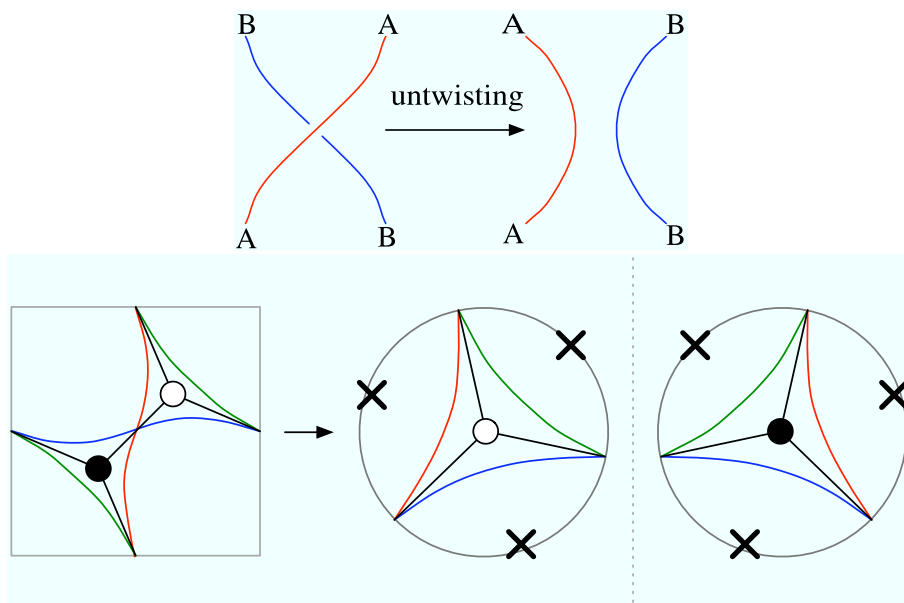
Figure 6: Untwisting. Two discs whose boundaries are identified represent a two-sphere. The crosses denote the punctures encircled by the 1-cycles.

and named the untwisting. When any two of the 1-cycles intersect in the alga, one locally untwists the intersection to obtain a new configuration. The result is precisely the amoeba. Figure 6 shows how the untwisting works for $\mathbb{C}^3$.

3.2 Geometry of Σ

As in the tiling model, we expect that the projections of the special Lagrangian manifold Σ will play a crucial role in the crystal model. As explained in section 2, supersymmetry requires that Σ be locally a product of a plane in $\mathbb{R}^3$ and a 1-cycle in T^3. Moreover, in order for Σ to be calibrated properly, the plane corresponding to a (p, q, r) 1-cycle should be orthogonal to a (p, q, r) vector in $\mathbb{R}^3$. Since Σ must be completely determined by the toric data, it is not difficult to guess what the planes and the 1-cycles are. Each edge $w_{IJ} = v_I - v_J$ of the toric diagram and the 2-fan orthogonal to the edge naturally give the plane/1-cycle pair.
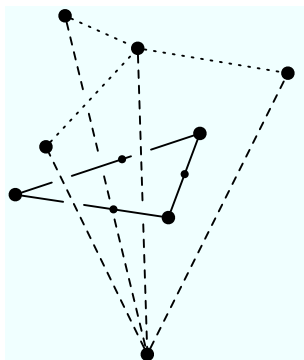
Figure 7: A part of the toric diagram. Each edge of the toric diagram corresponds to a 2-fan in $\mathbb{R}^3$ and a 1-cycle in T^3. Suppressing the radial direction, the 2-fans form the dual toric diagram.

Just as the amoeba in the tiling model is a thickened (p,q)-web and the boundary of the alga gave the $(q,-p)$ 1-cycles, we expect that the amoeba and the alga projections of the special Lagrangain manifold Σ in the crystal model will give a thickened 2-fans in $\mathbb{R}^3$ paired with 1-cycles in T^3. Unfortunately, to our knowledge, an explicit equation describing the shape of the special Lagrangian manifold Σ is not known,[1] but we can get some intuition from the following consideration.

Recall that the holomorphic surface for the tiling model was given by the Newton polynomial. If we write down the Newton polynomial for a CY_4 as in (3.1) but with three $\mathbb{C}^*$ variables, it is locally a product of a plane in $\mathbb{R}^3$ and a *2-cycle* in T^3. We now take the *mirror* of the $(C^*)^3$, that is, T-dualize along the T^3-fiber of $(\mathbb{C}^*)^3$, then we obtain a dual $(\mathbb{C}^*)^3$. If there were a D4-brane wrapping the holomorphic surface in the original $(\mathbb{C}^*)^3$, then it would be transformed into a D3-brane wrapping a special Lagrangian submanifold of the dual $(\mathbb{C}^*)^3$. We conjecture that this is precisely the Σ we are looking for. We should warn the readers that we are using mirror symmetry as a tool to relate a manifold to another, and it has nothing to do with the physical symmetry of the crystal model.

In the tiling model, it was useful to represent the amoeba as a punctured Riemann surface. The punctures are the points at infinity along the legs of the (p,q)-web. In the crystal model, we can also think of the amoeba of Σ as a 3-manifold with some defects. As we shrink the 2-fans along the radial direction, the 'points at infinity' form a locally one dimensional defect. The 1-cycles paired with the 2-fans are localized along the defects. Globally, the defect is isomorphic to the dual toric diagram. As we will see in the next subsection, when the toric diagram has no internal points, the amoeba has the topology of a three-sphere apart from the defect. It will be important to find out the topology of the amoeba in the general case in order to complete the inverse algorithm.

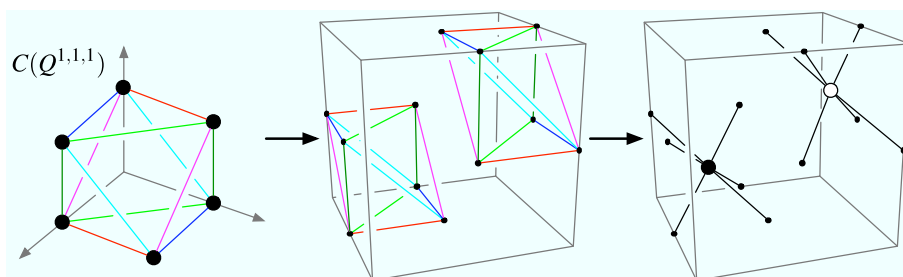## 3.3 The alga and the crystal

We now put together the contents of the previous two subsections to find the inverse algorithm for the crystal model. It is natural to expect that the alga projection of Σ onto

---

[1]We thank D. Joyce for a correspondence on this point.
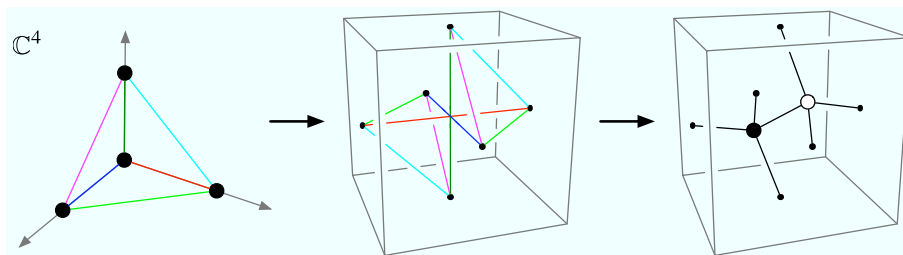
Figure 8: Each edge of the toric diagram gives a 1-cycle in the T^3. The 1-cycles define certain solids. The 1-cycles bend into the solids and merge to form the bonds and atoms of the crystal.


Figure 9: The crystal for $C(Q^{1,1,1})$ has the NaCl structure.

T^3 will again reveal the structure of the intersection between the Σ-brane and the T-branes. With no explicit equation describing Σ, we cannot derive the alga from a first principle. Nevertheless, in analogy with the tiling model, we can guess the shape of the alga and make consistency checks later.

Each edge of the toric diagram gives a 1-cycle in the T^3. Unlike in the tiling model, the 1-cycles generically do not intersect with each other. In order to fix the positions of the 1-cycles in the T^3, we make the following observation. When several edges form a boundary of a face of the toric diagram, the total homology charge of the corresponding 1-cycles vanish. Since the 2-fans meet with each other, the 1-cycles can join each other and be deformed smoothly into a vanishing cycle. Therefore, we require that the 1-cycles associated to a same face of the toric diagram intersect with one another in the T^3. In the simplest cases, this requirement is sufficient to construct the alga of a given CY$_4$. Figures 8 and 9 show the alga and the crystals for $\mathbb{C}^4$ and $C(Q^{1,1,1})$.

These crystals are particularly simple because all lattice points of the toric diagram are corners, that is, they do not lie in the interior, on the surfaces, or along the edges. In fact, when the toric diagram is a convex subset of a unit cube, there is a one-to-one correspondence between the vertices of the toric diagram and the bonds of the crystal. Note that figure 3(e) also falls into this class.

Applying the algorithm to orbifolds of $\mathbb{C}^4$ leads to slightly more complicated crystals. Figure 10 shows the crystal for $(\mathbb{C}^3/\mathbb{Z}_2 \times \mathbb{Z}_2) \times \mathbb{C}$ whose toric diagram is in figure 3(d). Note that, compared to the $\mathbb{C}^4$ case, the toric diagram is enlarged by a factor of 2 in the
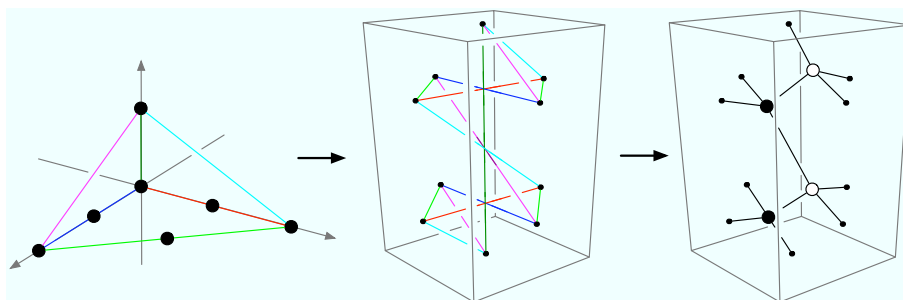
Figure 10: The crystal for $(\mathbb{C}^3/\mathbb{Z}_2 \times \mathbb{Z}_2) \times \mathbb{C}$.
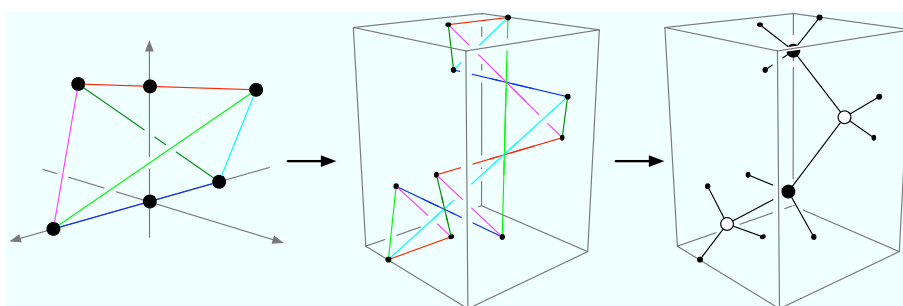
Figure 11: The crystal for $(\mathbb{C}^2/\mathbb{Z}_2)^2$.

x and y directions, while the unit cell in the crystal is twice as large in the z direction. So, in contrast to the tiling model, it is not straightforward to obtain the crystal for $(\mathbb{C}^3/\mathbb{Z}_m \times \mathbb{Z}_n) \times \mathbb{C}$ for arbitrary m and n.

Figure 11 shows the crystal for another orbifold, $(\mathbb{C}^2/\mathbb{Z}_2)^2$. Again, the crystal structure for the orbifolds is the same as that of $\mathbb{C}^4$, except that the unit cell is twice as large. The basis vectors of the new unit cells in terms of those of $\mathbb{C}^4$ are $(0,0,1)$, $(1,-1,0)$, $(1,1,-1)$.

3.4 Untwisting and the amoeba

In the tiling model, the untwisitng map reflects the fact that the real and imaginary parts of a holomorphic function are related to each other through the Cauchy-Riemann condition. As the special Lagrangian manifold Σ is a 'mirror' of a holomorphic surface, we expect that an analog of the untwisting map exists.

It is indeed possible to untwist the alga to obtain the amoeba which has all the properties we discussed earlier. Just as in the tiling model, the untwisting flips the orientation of the space transverse to the bond of the crystal. See figure 12. We apply the untwisting map to the alga of $\mathbb{C}^4$, we obtain the amoeba depicted in figure 13. Note that the dual toric diagram is a tetrahedron as expected. The 1-cycles are localized along the dual toric diagram as they should be. Applying the untwisting map to $C(Q^{1,1,1})$ yields a similar result, with the dual toric diagram being a cube.
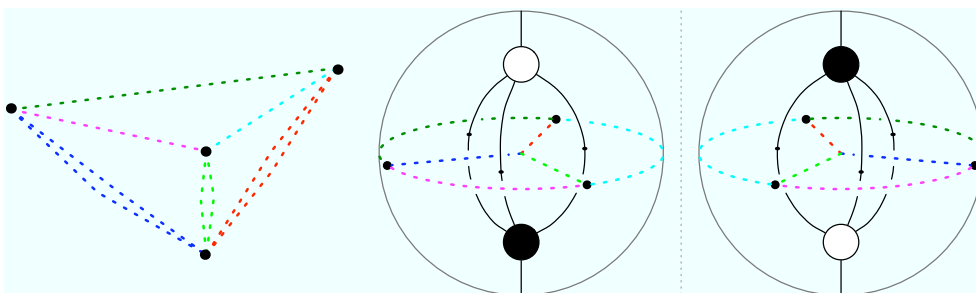
The untwisting map for the orbifolds is more non-trivial. The dual toric diagrams have
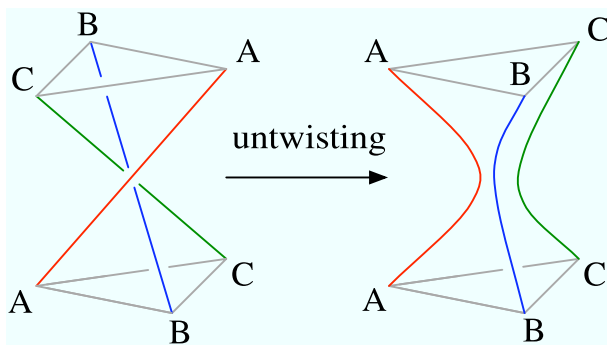
Figure 12: Untwisting the crystal.
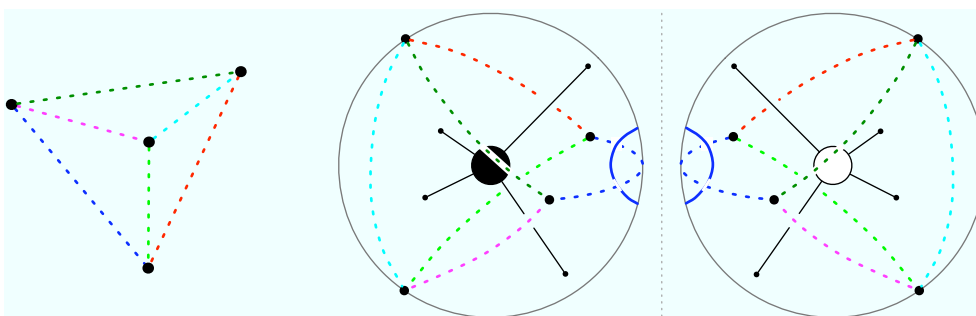
Figure 13: Amoeba for $\mathbb{C}^4$. We represent a three-sphere as the union of two balls with the surfaces identified. The dotted lines on the balls denote defects.

Figure 14: The dual toric diagram and its embedding into the amoeba for $(\mathbb{C}^3/\mathbb{Z}_2 \times \mathbb{Z}_2) \times \mathbb{C}$.

double-lines because some points of the toric diagrams sit on the edges. It is a priori not clear how the double line should split in the amoeba. The untwisting map answers the question.

4. Forward algorithm

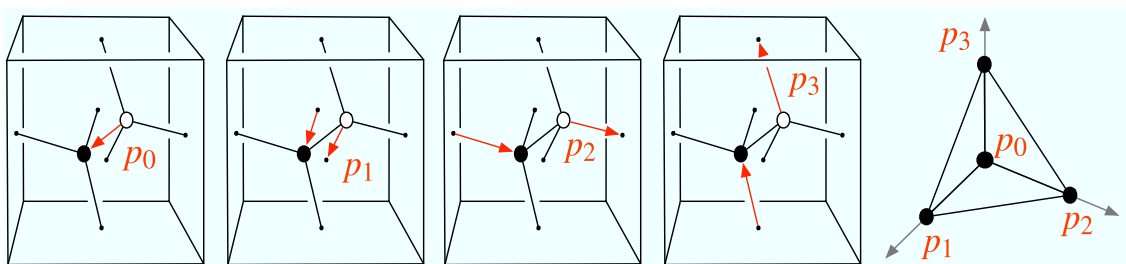The forward algorithm of the tiling model as described in [1] is based on two related notions, namely, perfect matchings and the Kasteleyn matrix. In this section, we show that the
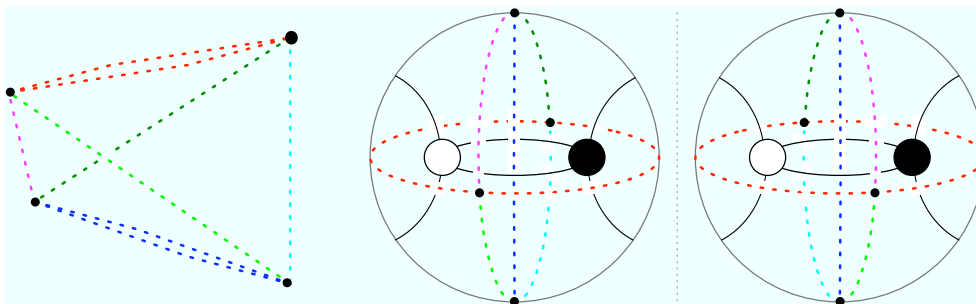
Figure 15: The dual toric diagram and its embedding into the amoeba for $(\mathbb{C}^2/\mathbb{Z}_2)^2$.

Figure 16: Perfect matchings of the crystal for $\mathbb{C}^4$

same tools work equally well for the crystal model with little modification.
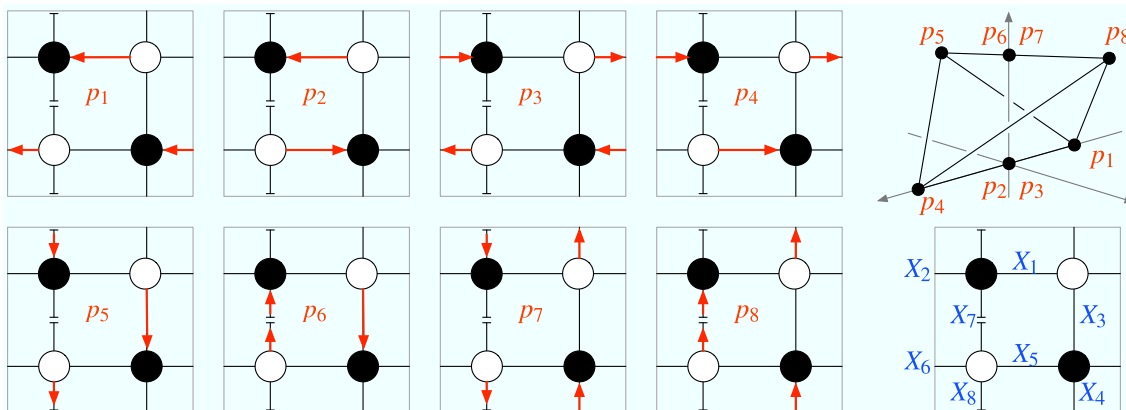
4.1 Perfect matchings

The concept of perfect matchings plays a crucial role in the forward algorithm. A perfect matching is a subset of bonds of the crystal, such that every atom of the crystal is an endpoint of precisely one such bond. The bonds in each perfect matching carry an orientation. We choose to orient the arrows to go from a white atom to a black one.

In the tiling model, perfect matchings are known to have several nice properties. In this section, we show that the same is true of the crystal model. We focus on two of the main features:

1. Each perfect matching can be located in the toric diagram. The relative coordinate in the toric diagram between two perfect matchings p_α and p_β is given by the homology charge of $(p_\alpha - p_\beta)$ regarded as a one-cycle in T^3.

2. The perfect matchings solve the 'abelian' version of the F-term condition for the chiral fields X_i associated to the bonds, if we set

$$X_i = \prod_\alpha p_\alpha^{\langle X_i, p_\alpha \rangle}, \tag{4.1}$$

where $\langle X_i, p_\alpha \rangle$ equals 1 if p_α contains the bond X_i and 0 otherwise.

Figure 17: Perfect matchings of the crystal for $(\mathbb{C}^2/\mathbb{Z}_2)^2$ projected onto the xy-plane. The short double lines on X_7, X_8 means that they go over different unit cells in the z-direction.

Instead of giving a general proof, we illustrate the idea with simple, but non-trivial, examples. When the crystal contains only two atoms, as is the case for $\mathbb{C}^4$ and $C(Q^{111})$, each and every bond in the crystal corresponds to a perfect matching. Figure 16 shows the four perfect matchings of the $\mathbb{C}^4$ crystal and how they are associated to points on the toric diagram. For any pair of perfect matchings p_α and p_β, the oriented path $(p_\alpha - p_\beta)$ forms a one-cycle in T^3. The homology charge translates into the relative coordinate between the two points corresponding to p_α and p_β. Since there are only two atoms, the F-term condition equates the product of all bonds meeting at an atom with the same product at the other atom. So, the abelian F-term condition is trivially satisfied.

The map between perfect matchings and points in the toric diagram becomes less trivial as the number of atoms increases. Figure 17 shows the eight perfect matchings of the $(\mathbb{C}^2/\mathbb{Z}_2)^2$ crystal and their location in the toric diagram. The F-term condition states that the product of bonds meeting at any atom is the same. Labeling the bonds as in the figure, the condition reads

$$X_1 X_2 X_3 X_4 = X_3 X_4 X_5 X_6 = X_5 X_6 X_7 X_8 = X_7 X_8 X_1 X_2. \tag{4.2}$$

It is easy to check that (4.1) solves this constraint. Explicitly,

$$X_1 = p_1 p_2, \quad X_2 = p_3 p_4, \quad X_3 = p_5 p_6, \quad X_4 = p_7 p_8,$$
$$X_5 = p_2 p_4, \quad X_6 = p_1 p_3, \quad X_7 = p_6 p_8, \quad X_8 = p_5 p_7. \tag{4.3}$$

The relation (4.1) also allows us to determine the charges of the fields X_i. The corners of the toric diagram correspond to baryons, and their charges can be computed from the volume of the associated supersymmetric 5-cycles. If we assign the charges to the corresponding perfect matchings and set the charges of other perfect matchings to zero, then (4.1) determines the charges of the fields X_i. Moreover, the super-potential terms contain each and every corner precisely once, so that their R-charges are always 2.

As a final remark, we note that just as in the tiling model, one can use the Kasteleyn determinant as a generating function of the perfect matchings.

4.2 Relation between the linear sigma model and the associated crystal

From the toric diagram of $C(Q^{1,1,1})$ in figure 3, one has the following toric vertices

$$v_1 = (1,0,0,1), \quad v_2 = (0,1,0,1), \quad v_3 = (1,1,0,1),$$
$$v_4 = (0,0,1,1), \quad v_5 = (1,0,1,1), \quad v_6 = (0,1,1,1). \tag{4.4}$$

From the relation (2.2) one can easily find the charges of the linear sigma model fields σ_I corresponding to v_I since in this case there are one to one correspondence between the perfect matchings and the vertices of the toric diagram. The charge vectors for σ_I are given by

$$Q_1 = (1,1,-1,-1,0,0),$$
$$Q_2 = (0,0,1,1,-1,-1). \tag{4.5}$$

The two charge assignments are the usual ones for the sigma model describing $C(Q^{1,1,1})$.

If we go to more complicated examples such as $\mathbb{C}^2/\mathbb{Z}_2 \times \mathbb{C}^2/\mathbb{Z}_2$, we have eight perfect matchings so that the symplectic quotients are described by $U(1)^4$ gauge theory with suitably charged matters. One can obtain the charge matrices for eight perfect matching fields again using the relation (2.2). However there are ambiguities in the charge assignments since one can think of various different $U(1)$ combinations in describing the same symplectic quotients. In the tiling model, the charge assignments arise naturally. The linear sigma model fields are suitable combinations of bifundamental fields appearing in the D-branes located in the considered Calabi-Yau singualrities. Here the relation between the fundamental excitations of membrane and the linear sigma model fields is not clear. We introduce the fields assigned with bonds and they are related to the prefect matchings. It is desirable to understand this issue better.

## 4.3 Trivalent atoms and non-uniqueness of the crystal

In the tiling model, a vertex with only two edges correspond to a mass term in the gauge theory. Integrating out the mass term translates into shrinking the vertex and the two edges away completely from the tiling. It is likely that the same is true of the crystal model, since as we will discuss in the next section, the atoms of crystals are interpreted as super-potential terms.

Unlike in the tiling model, trivalent atoms of the crystal model also deserve special attention. As discussed in section 2, in the inverse algorithm, the atoms appear from solid components of the alga. A proper three dimensional solid has at least four vertices, which means that the resulting atom should have at least four bonds. It is still conceivable that trivalent atoms appear as the solid is somehow 'squashed' to lie in a plane. In fact, we have found several crystals with trivalent atoms. Although the inverse algorithm suggests that they are rather unnatural, so far we have not found any physical inconsistency to rule them out.

The first example of a crystal with trivalent bonds comes from the orbifold $\mathbb{C}^2/\mathbb{Z}_2 \times \mathbb{C}^2$ whose toric diagram is given in figure 3(b) and crystal depicted in figure 18. It is easy to
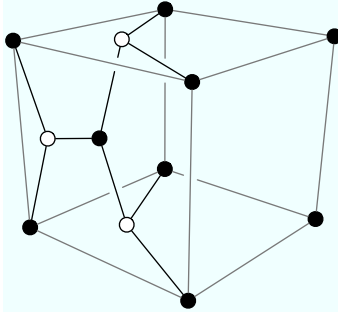
Figure 18: The crystal for $\mathbb{C}^2/Z_2 \times \mathbb{C}^2$.

(a) (b)
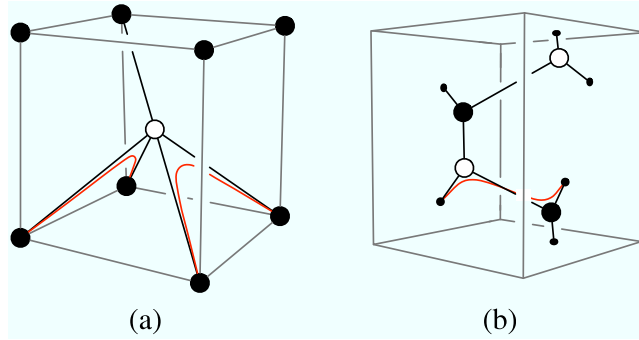
**Figure 19:** The two crystals for $C(T^{1,1}) \times \mathbb{C}$.

check that the crystal can reproduce the toric diagram with the perfect matching. The R-charges can be assigned to the bonds as before.

Another interesting example is $C(T^{1,1}) \times \mathbb{C}$. Its toric diagram is described in figure 3(e). This is our first example having two different crystals; see figure 19. The crystal (a) is derived from the inverse algorithm just as the $\mathbb{C}^4$ and $C(Q^{1,1,1})$ examples discussed in section 3, and does not contain any trivalent atom. The crystal (b), on the other hand, contains trivalent atoms only. Both crystals give the same toric diagram as far as the perfect matching method is concerned.

To determine whether both crystals are physically relevant will require a more thorough understanding of the inverse algorithm. In the tiling model, two or more tilings corresponding to the same toric diagram are known to be related to each other by Seiberg duality. So, if two or more crystals are indeed allowed, we will have to find out an analog of Seiberg duality in the new setup.

The crucial difference between two crystals is that the crystal (a) has two homology $(1, 0, 0)$ 1-cycles as shown in the figure 19 (red curves), but the other one has only one such 1-cycle. It can be understood that two 1-cycles in the crystal (a) are degenerate in the crystal (b). In the tiling model, degenerate 1-cycles often lead to inconsistent dimer graphs. Even though degenerate cycles do not lead to an inconsistent crystal, we may say that the crystal containing trivalent atoms is more singular based on the degenerate 1-cycles.
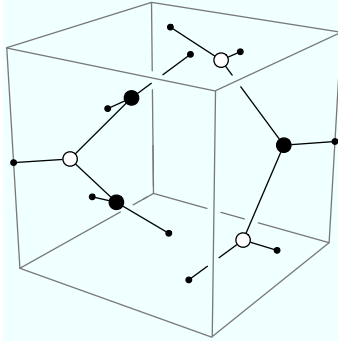
Figure 20: A candidate for the $C(M^{3,2})$ crystal.
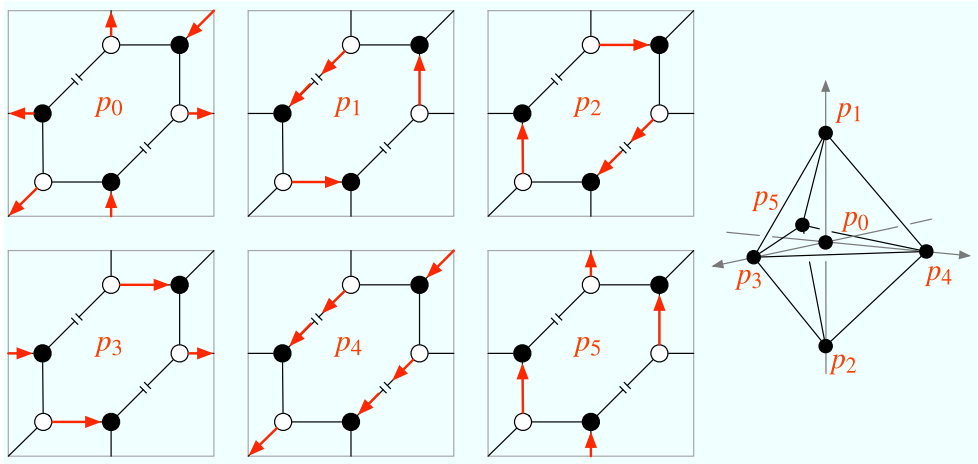
Figure 21: Perfect matchings of the $C(M^{3,2})$ crystal candidate, projected onto the xy-plane.

We close this subsection with a proposal for the crystal structure of $C(M^{32})$, whose toric diagram is given in figure 3(g). With our limited understanding of the inverse algorithm, we have not been able to derive the crystal for $C(M^{3,2})$ from the toric diagram. It is still possible to do some guesswork to find a candidate and check whether it gives the correct toric diagram using the perfect matchings. Figure 20 shows one such candidate. As shown in figure 21, the perfect matchings do yield the toric diagram of $C(M^{3,2})$.

However, the crystal consists of trivalent atoms only. If we check the R-charges of the bonds of the crystal, all six edges of the 'hexagon' in the interior of the unit cell are contained in degenerate 1-cycles in the sense we discussed above. There may exist a more regular crystal without trivalent atoms. We hope to resolve this issue in a future work.

5. Counting BPS meson states

Counting BPS states is one of the most basic problems in AdS/CFT with supersymmetry. Very much progress has been made recently in counting states preserving a half of the supersymmetry in $D = 4$, $\mathcal{N} = 1$ [40, 41, 10–18] or $D = 3$, $\mathcal{N} = 2$ theories [13, 42].

Exact partition functions for mesons and baryons have been written down. In the crystal model, the BPS meson states are represented by closed membrane configurations. In this section, we explain in detail how the crystal model correctly reproduces the meson spectrum computed on the geometry side.

5.1 Character functions

Chiral mesons in CFT_3 correspond to algebraic (holomorphic polynomial) functions on the CY_4 cone X. They are labeled by integer points $m = (m_1, m_2, m_3, m_4)$ in the solid cone Δ, which are the momentum quantum numbers along the T^4 fiber of X. It follows immediately that the flavor charges of a meson m are $F_i(m) = m_i$. The R-charge of the meson is then given by [8, 10, 43]

$$R(m) = \frac{1}{2}b^i F_i(m) = \frac{1}{2}(m \cdot b). \tag{5.1}$$

The spectrum of all mesons is conveniently summarized in the character function [10, 11].

$$Z(q_i; X) \equiv \sum_{\{m\}} \prod_{i=1}^{4} q_i^{m_i} \tag{5.2}$$

When the CY_4 is toric, a closed form of the character function can be read off from the toric diagram. One draws the graph dual of a triangulation of the toric diagram. The result is a tetra-valent graph whose external legs are the 1-fans discussed in section 2. Then the partition functions is given by

$$Z(q_i; X) = \sum_{\alpha \in T} \prod_{b=1}^{4} \frac{1}{1 - \prod q_i^{a_{\alpha b}^i}}. \tag{5.3}$$

The sum runs over the vertices of the graph or, equivalently, the simplexes of the triangulation. The product runs over the four edges $\vec{a}_{\alpha b}$ meeting at the vertex α. See [10, 11] for more details. Applying this formula to the examples of the current paper, we find

$$\mathbb{C}^4 : \frac{1}{(1-q_1)(1-q_2)(1-q_3)(1-q_4/q_1 q_2 q_3)}, \tag{5.4}$$

$$\mathbb{C}^2/\mathbb{Z}_2 \times \mathbb{C}^2 : \frac{1 + q_4/q_1 q_2}{(1-q_1)(1-q_2)(1-q_3 q_4/q_1 q_2)(1-q_4/q_1 q_2 q_3)}, \tag{5.5}$$

$$(\mathbb{C}^2/\mathbb{Z}_2)^2 : \frac{(1+q_3)(1+q_4/q_3)}{(1-q_1 q_3)(1-q_3/q_1)(1-q_2 q_4/q_3)(1-q_4/q_2 q_3)}, \tag{5.6}$$

$$\mathbb{C}^2/(\mathbb{Z}_2 \times \mathbb{Z}_2) \times \mathbb{C} : \frac{1 + q_4/q_3}{(1-q_1)(1-q_2)(1-q_3)(1-q_4{}^2/q_1 q_2 q_3{}^2)}, \tag{5.7}$$

$$C(T^{1,1}) \times \mathbb{C} : \frac{1 - q_4/q_3}{(1-q_1)(1-q_2)(1-q_3)(1-q_4/q_1 q_3)(1-q_4/q_2 q_3)}, \tag{5.8}$$

and similar expressions for $C(Q^{1,1,1})$ and $C(M^{3,2})$. The volume of the base of the cone, Y, can be obtained from the character functions [10].

$$\frac{\text{Vol}(Y)}{\text{Vol}(S^7)} = \lim_{t \to 0} t^4 Z(e^{-b^i t}; X = C(Y)). \tag{5.9}$$

The value of the Reeb vector which renders Y Einstein (or, equivalently, X Ricci-flat), can be determined by minimizing the volume [27]. Inserting the value back to the character function by $q_i \to q^{\frac{b^i}{2}}$, we find the level surface, that is, we can count the degeneracy of mesons at each value of the R-charge. For $\mathbb{C}^4$ and its orbifolds, the result is:

$$\mathbb{C}^4 : \frac{1}{(1-q^{1/2})^4}, \qquad \mathbb{C}^2/\mathbb{Z}_2 \times \mathbb{C}^2 : \frac{1+q}{(1-q)^2(1-q^{1/2})^2}, \qquad (5.10)$$

$$(\mathbb{C}^2/\mathbb{Z}_2)^2 : \frac{(1+q)^2}{(1-q)^4}, \qquad (\mathbb{C}^3/\mathbb{Z}_2 \times \mathbb{Z}_2) \times \mathbb{C} : \frac{1+q^{3/2}}{(1-q)^3(1-q^{1/2})}. \qquad (5.11)$$

For other examples we have been studying, the answer is:

$$C(T^{1,1}) \times \mathbb{C} : \frac{1+q^{3/4}}{(1-q^{3/4})^3(1-q^{1/2})} = 1 + q^{\frac{1}{2}} + 4q^{\frac{3}{4}} + \cdots, \qquad (5.12)$$

$$C(Q^{1,1,1}) : \frac{1+4q+q^2}{(1-q)^4} = \sum_k (k+1)^3 q^k, \qquad (5.13)$$

$$C(M^{3,2}) : \frac{(1+q^2)(1+25q^2+q^4)}{(1-q^2)^4} = \sum_k (2k+1)\frac{(3k+1)(3k+2)}{2}q^{2k}. \qquad (5.14)$$

The last two results agree with other methods used previously to obtain the spectrum [34].

5.2 Mesons as closed membranes

Consider an atom with several bonds. If we add up all the M2 discs localized along the bonds with a fixed orientation, we obtain a spherical membrane surrounding the atom. In analogy with the tiling model, we identify such a configuration as a super-potential term of the CFT_3. The R-charge and the flavor charges of the spherical M2-brane is the sum of the charges of the component M2-discs. The super-potential terms should have R-charge two and vanishing flavor charges. As pointed out in [25], it is true because (i) every atom corresponds to a partition covering the entire toric diagram (ii) the sum of charges over all 3-fans is either two (R-charge) or zero (flavor charges) due to the toric relations.

The super-potential terms yield the F-term equivalence relations among the elements of the chiral ring. As in the tiling model, the relations imply that the sum of terms corresponding to any two connected atoms are F-term equivalent to zero. Put another way, a spherical M2-brane wrapping a white atom in the crystal is F-term equivalent to another M2-brane wrapping a black atom with opposite orientation as illustrated in figure 22. This is why we painted the atoms in two colors in the first place. Hence the tiling model and the crystal model share the notions of a bipartite graph and dimers.

We make a short digression to what the crystal model implies for the field theory description of CFT_3. An attempt was made in [34] to write down quiver gauge theories dual to $AdS_4 \times Q^{1,1,1}$. The proposed theory contained six chiral superfields $(A_1, A_2, B_1, B_2, C_1, C_2)$, where A_i, B_i, C_i are doublets under the three $SU(2)$ global symmetries. It was shown that the Kaluza-Klein spectrum and the baryon spectrum can be reproduced from these fields if one assumes a certain symmetrization rule. In CFT_4, the symmetrization rule follows from the super-potential through the F-term condition. The authors of [34] found that the
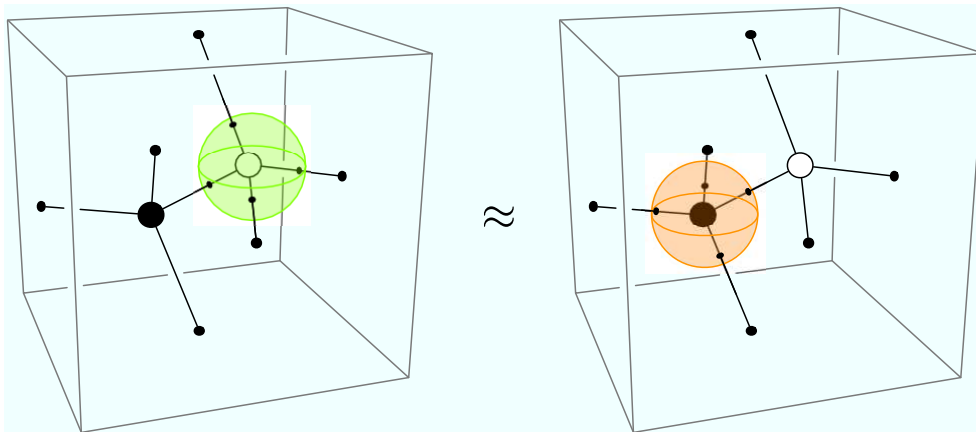
Figure 22: Super-potential terms as spherical M2-branes surrounding the atoms. The F-term condition equates a closed M2-brane wrapping a white atom to another M2-brane wrapping a black atom with the opposite orientation.

unique candidate for the super-potential with the correct quantum numbers vanishes identically. The crystal model reveals the origin of the problem. The crystal for $C(Q^{1,1,1})$ has precisely six fundamental M2-discs that matches the field content mentioned above. Now, the M2-discs form the super-potential terms over a sphere. This geometry cannot be represented by a trace of product of matrices; matrices represent strings with two end-points. The correct description of CFT$_3$ would require an algebraic expression beyond matrices.

Recall that the mesons of CFT$_3$ are KK momentum modes in AdS$_4 \times Y$, and are labeled by integer points m in the solid cone Δ. T-duality transforms the mesons into closed M2-branes. As shown in [25], the first three components of m define the homology charge of the 2-cycle in the T^3 that the M2-meson is wrapping. The last component of m, contributing $2m_4$ to the R-charge, measures how many times the M2-meson wraps a super-potential term. The F-term condition ensures that all the M2-meson with the same value of m are F-term equivalent, regardless of the precise way they wrap the atoms. So there is a unique meson for each value of m, in accord with the results from the geometric side we reviewed in the last subsection.

It is instructive to check the main assertions of this subsection in explicit examples. The mesons of $\mathbb{C}^4$ at $R = k/2$ form a k-fold totally symmetric tensor representation of the SU(4) global symmetry. At $k = 1$, the four mesons are $m = (1,0,0,0)$, $(0,1,0,0)$, $(0,0,1,0)$ and $(-1,-1,-1,1)$. Figure 23 depicts the 2-cycles representing the mesons, where we again use colors to denote the orientation of the 2-cycles.

For $C(T^{1,1}) \times \mathbb{C}$, the lowest lying meson has $m = (0,0,1,0)$ and $R = 1/2$. It has the same shape as the third meson in figure 23. At the next level, we have four states with $R = 3/4$. They are shown in figure 24.

So far, we have considered only the single meson states with arbitrary values of m. In gauge theory terms, we have concentrated on 'single trace' meson operators in the large N limit. It would be interesting to include baryons and take the finite N effect into account.
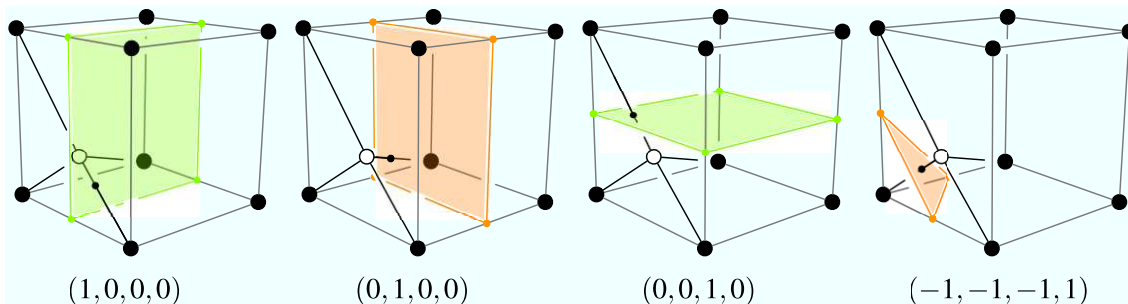
Figure 23: Mesons of $\mathbb{C}^4$ with $R = 1/2$.
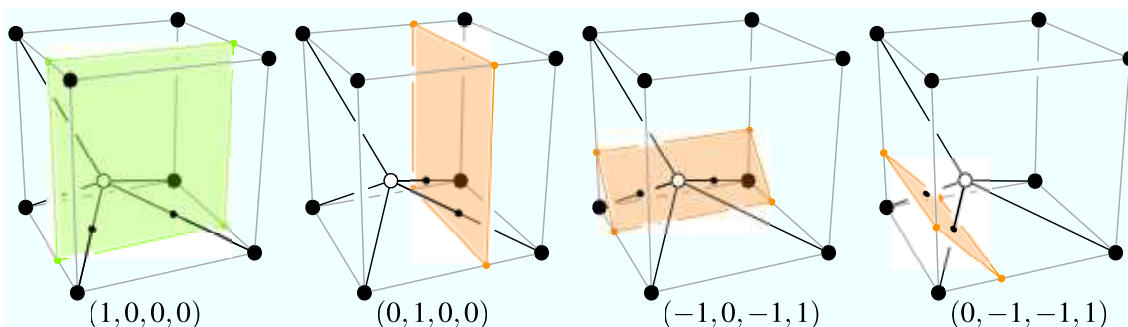
Figure 24: Mesons of $C(T^{1,1}) \times \mathbb{C}$ with $R = 3/4$.

6. Discussion

In this paper, we studied in some detail the map between a toric CY_4 and the corresponding crystal model. Compared to the tiling model, the map is incomplete in many aspects. One of the most important gap to fill in is an explicit description of the special Lagrangian manifold Σ. If found, it will prove (or disprove) rigorously the assertions concerning the inverse algorithm and possibly reveal more structures. It may also answer some of the questions we encountered such as the role of trivalent atoms and the relation between different crystals for the same CY_4.

It is by now well-known that a few simple formulas hold for the tiling model. The number of tiles is twice the area of the toric diagram. The genus of the amoeba is equal to the number of internal points of the toric diagram. The total number of edges of the tiling is given by

$$\sum_{I<J} \left| \det \begin{pmatrix} p_I & q_I \\ p_J & q_J \end{pmatrix} \right|, \tag{6.1}$$

where the sum runs over all legs of the (p,q)-web. It will be nice to find out whether these relations have a counterpart in the crystal model.

We considered only a limited number of examples in this paper. It is certainly desirable to study more examples and relations among them. In the study of the tiling model, partial

resolutions of a CY_3 to obtain another less singular CY_3 has proved quite useful. In the simplest case, partial resolution in the tiling model removes some of the edges of the tiling. A preliminary study shows that the same is true of the crystal model, but a systematic method is yet to be developed. As in [21], it is likely that the amoeba projection and the untwisting map will again play an essential role.

Marginal deformation of the CFT_3 is another important subject. In [44], the derivation of the β-deformed geometry of toric CY_4 cones tacitly anticipated the crystal model for CFT_3. The same paper also explained how to interpret the phase factors attached to each terms in the super-potential using a sort of $\star$-product. The $\star$-product involves the flavor charges of the bi-fundamental fields. It would be interesting to give a similar interpretation to the β-deformation of CFT_3 [44, 37, 38]. To do so, we will need to define an analog of the $\star$-product for membranes, perhaps along the line of [45].

References

[1] A. Hanany and K.D. Kennaway, *Dimer models and toric diagrams*, `hep-th/0503149`.

[2] S. Franco, A. Hanany, K.D. Kennaway, D. Vegh and B. Wecht, *Brane dimers and quiver gauge theories*, *JHEP* **01** (2006) 096 [`hep-th/0504110`].

[3] S. Franco et al., *Gauge theories from toric geometry and brane tilings*, *JHEP* **01** (2006) 128 [`hep-th/0505211`].

[4] A. Hanany and D. Vegh, *Quivers, tilings, branes and rhombi*, `hep-th/0511063`.

[5] B. Feng, Y.-H. He, K.D. Kennaway and C. Vafa, *Dimer models from mirror symmetry and quivering amoebae*, `hep-th/0511287`.

[6] A. Hanany, C.P. Herzog and D. Vegh, *Brane tilings and exceptional collections*, *JHEP* **07** (2006) 001 [`hep-th/0602041`].

[7] A. Butti, *Deformations of toric singularities and fractional branes*, *JHEP* **10** (2006) 080 [`hep-th/0603253`].

[8] A. Butti, D. Forcella and A. Zaffaroni, *Deformations of conformal theories and non-toric quiver gauge theories*, *JHEP* **02** (2007) 081 [`hep-th/0607147`].

[9] Y. Imamura, H. Isono, K. Kimura and M. Yamazaki, *Exactly marginal deformations of quiver gauge theories as seen from brane tilings*, `hep-th/0702049`.

[10] D. Martelli, J. Sparks and S.-T. Yau, *Sasaki-Einstein manifolds and volume minimisation*, `hep-th/0603021`.

[11] S. Benvenuti, B. Feng, A. Hanany and Y.-H. He, *Counting BPS operators in gauge theories: quivers, syzygies and plethystics*, `hep-th/0608050`.

[12] D. Martelli and J. Sparks, *Dual giant gravitons in Sasaki-Einstein backgrounds*, *Nucl. Phys.* **B 759** (2006) 292 [`hep-th/0608060`].

[13] A. Basu and G. Mandal, *Dual giant gravitons in $AdS_m \times Y^n$ (Sasaki-Einstein)*, `hep-th/0608093`.

[14] A. Butti, D. Forcella and A. Zaffaroni, *Counting BPS baryonic operators in CFTs with Sasaki-Einstein duals*, `hep-th/0611229`.

[15] A. Hanany and C. Romelsberger, *Counting BPS operators in the chiral ring of $N = 2$ supersymmetric gauge theories or $N = 2$ braine surgery*, `hep-th/0611346`.

[16] L. Grant and K. Narayan, *Mesonic chiral rings in Calabi-Yau cones from field theory*, `hep-th/0701189`.

[17] D. Forcella, A. Hanany and A. Zaffaroni, *Baryonic generating functions*, `hep-th/0701236`.

[18] B. Feng, A. Hanany and Y.-H. He, *Counting gauge invariants: the plethystic program*, *JHEP* **03** (2007) 090 [`hep-th/0701063`].

[19] D.R. Morrison and M.R. Plesser, *Non-spherical horizons. I*, *Adv. Theor. Math. Phys.* **3** (1999) 1 [`hep-th/9810201`].

[20] J. Park, R. Rabadán and A.M. Uranga, *Orientifolding the conifold*, *Nucl. Phys.* **B 570** (2000) 38 [`hep-th/9907086`].

[21] I. Garcia-Etxebarria, F. Saad and A.M. Uranga, *Quiver gauge theories at resolved and deformed singularities using dimers*, *JHEP* **06** (2006) 055 [`hep-th/0603108`].

[22] I. Garcia-Etxebarria, F. Saad and A.M. Uranga, *Local models of gauge mediated supersymmetry breaking in string theory*, *JHEP* **08** (2006) 069 [`hep-th/0605166`].

[23] S. Franco and A.M. . Uranga, *Dynamical SUSY breaking at meta-stable minima from D-branes at obstructed geometries*, *JHEP* **06** (2006) 031 [`hep-th/0604136`].

[24] S. Franco, A. Hanany, F. Saad and A.M. Uranga, *Fractional branes and dynamical supersymmetry breaking*, *JHEP* **01** (2006) 011 [`hep-th/0505040`].

[25] S. Lee, *Superconformal field theories from crystal lattices*, `hep-th/0610204`.

[26] D. Martelli and J. Sparks, *Toric geometry, Sasaki-Einstein manifolds and a new infinite class of AdS/CFT duals*, *Commun. Math. Phys.* **262** (2006) 51 [`hep-th/0411238`].

[27] D. Martelli, J. Sparks and S.T. Yau, *The geometric dual of a-maximisation for toric Sasaki-Einstein manifolds*, *Commun. Math. Phys.* **268** (2006) 39 [`hep-th/0503183`].

[28] S. Lee and S.-J. Rey, *Comments on anomalies and charges of toric-quiver duals*, *JHEP* **03** (2006) 068 [`hep-th/0601223`].

[29] D. Berenstein, C.P. Herzog and I.R. Klebanov, *Baryon spectra and AdS/CFT correspondence*, *JHEP* **06** (2002) 047 [hep-th/0202150].

[30] L. Castellani, L.J. Romans and N.P. Warner, *A classification of compactifying solutions for D = 11 supergravity*, *Nucl. Phys.* **B 241** (1984) 429.

[31] L. Castellani et al., *G/H M-branes and AdS(p + 2) geometries*, *Nucl. Phys.* **B 527** (1998) 142 [hep-th/9803039].

[32] C.-h. Ahn and H. Kim, *Branes at C(4)/Γ singularity from toric geometry*, *JHEP* **04** (1999) 012 [hep-th/9903181].

[33] G. Dall'Agata, *N = 2 conformal field theories from M2-branes at conifold singularities*, *Phys. Lett.* **B 460** (1999) 79 [hep-th/9904198].

[34] D. Fabbri et al., *3d superconformal theories from sasakian seven-manifolds: new nontrivial evidences for AdS₄/CFT₃*, *Nucl. Phys.* **B 577** (2000) 547 [hep-th/9907219].

[35] C.-h. Ahn, *N = 2 SCFT and M-theory on AdS₄ × Q(1,1,1)*, *Phys. Lett.* **B 466** (1999) 171 [hep-th/9908162].

[36] J.P. Gauntlett, D. Martelli, J.F. Sparks and D. Waldram, *A new infinite class of Sasaki-Einstein manifolds*, *Adv. Theor. Math. Phys.* **8** (2006) 987 [hep-th/0403038].

[37] C.-h. Ahn and J.F. Vazquez-Poritz, *Marginal deformations with* $\mathrm{U}(1)^3$ *global symmetry*, *JHEP* **07** (2005) 032 [hep-th/0505168].

[38] J.P. Gauntlett, S. Lee, T. Mateos and D. Waldram, *Marginal deformations of field theories with AdS₄ duals*, *JHEP* **08** (2005) 030 [hep-th/0505207].

[39] Y. Imamura, *Global symmetries and 't Hooft anomalies in brane tilings*, *JHEP* **12** (2006) 041 [hep-th/0609163].

[40] I. Biswas, D. Gaiotto, S. Lahiri and S. Minwalla, *Supersymmetric states of N = 4 Yang-Mills from giant gravitons*, hep-th/0606087.

[41] G. Mandal and N.V. Suryanarayana, *Counting 1/8-BPS dual-giants*, *JHEP* **03** (2007) 031 [hep-th/0606088].

[42] S. Bhattacharyya and S. Minwalla, *Supersymmetric states in M5/M2 CFTs*, hep-th/0702069.

[43] J.P. Gauntlett, D. Martelli, J. Sparks and S.-T. Yau, *Obstructions to the existence of Sasaki-Einstein metrics*, hep-th/0607080.

[44] O. Lunin and J.M. Maldacena, *Deforming field theories with* $\mathrm{U}(1) \times \mathrm{U}(1)$ *global symmetry and their gravity duals*, *JHEP* **05** (2005) 033 [hep-th/0502086].

[45] P.-M. Ho and Y. Matsuo, *A toy model of open membrane field theory in constant 3-form flux*, hep-th/0701130.